

# A Predictive Controller for Drivability and Comfort in Multi-Motor Electric Vehicles

Chen, Di; Danielson, Claus; Di Cairano, Stefano

TR2021-133 November 13, 2021

## Abstract

This paper presents a robust rate-based model predictive control (rate-based MPC) for controlling electric vehicle (EV) with independently actuated wheels and anti-squat/lift/dive suspensions. We present steps by which we arrive at a controller with good tracking performance, the capability to improve passenger comfort by reducing the lift, pitch, and roll motion of the vehicle chassis, and the ability to modify the reference to maintain vehicle lateral stability. CarSim simulation results are presented that demonstrate the ability of rate-based MPC to achieve good longitudinal acceleration and yaw rate tracking while reducing the suspension motions, despite the discrepancy between the high-fidelity CarSim model and the control-oriented model.

*IFAC Modeling, Estimation and Control Conference (MECC) 2021*



# A Predictive Controller for Drivability and Comfort in Multi-Motor Electric Vehicles

Di Chen \* Claus Danielson \*\* Stefano Di Cairano \*\*\*

\* *University of Michigan (dichen@umich.edu)*

\*\* *University of New Mexico, (cdanielson@unm.edu)*

\*\*\* *Mitsubishi Electric Research Labs (dicairano@ieee.org)*

---

**Abstract:** We present a robust rate-based model predictive control (rate-based MPC) for controlling electric vehicle (EV) with independently actuated wheels and anti-squat/lift/dive suspensions that achieves drivability, i.e., good tracking performance, improved passenger comfort, i.e., reduction of chassis lift, pitch, and roll, and increased vehicle lateral stability. The controller is validated in closed-loop with CarSim demonstrating robustness to model errors between the high-fidelity CarSim simulation model and the control-oriented prediction model.

*Keywords:* Electric Vehicle; Chassis Control; Model Predictive Control; Robust control

---

## 1. INTRODUCTION

Besides the positive impact on “decarbonization” electric vehicles (EVs) may provide additional advantages. EVs with multiple smaller electric motors, instead of a traditional monolithic drivetrain, can vector traction forces, which can be used to improve vehicle handling, stability, and responsiveness (Wang et al., 2015; Nahidi et al., 2017).

In (Chen et al., 2020), we explored using independently actuated wheels to improve passenger comfort by reducing the chassis motion. In this paper, we develop a control design that jointly achieve reduction of chassis motion and vehicle responsiveness. An EV with four independently actuated wheels has five control inputs, the “throttle” for each wheel and the steering angle. Vehicle drivability, which amounts to the vehicle rapidly and predictably responding to drivers commands, requires precise and fast tracking of two reference outputs, vehicle acceleration and yaw-rate. Thus, three degrees-of-freedom remain that can be used to improve passenger comfort by reducing the pitch, roll, and lift motion of the chassis.

Most research on EV chassis control has focused on improving reference tracking, lateral stability, and handling, hence using planar vehicle models (Wang et al., 2015; Nahidi et al., 2017). (Ochi et al., 2013) proposed a model describing the vehicle’s roll motion based on anti-dive/squat suspensions, and designed a controller for lateral stability and chassis roll reduction, for comfort during cornering. (Zhang and Wang, 2015) a gain-scheduled linear feedback for active front-wheel steering and direct yaw moment control for lateral control when longitudinal velocity varies, yet without considering chassis motion. Relatively few works considers EV motors for improve comfort (see (Chen et al., 2020) and the references therein), for which usually semi-active/active suspension systems are often investigated. (Zhao et al., 2019) proposed a hierarchical integrated control based on sliding mode, for vehicle longitudinal, lateral, and vertical dynamics where the chassis motion control is achieved mainly by active

suspensions. However, these may not be widely used due to higher cost and possibly reduced durability, while semi-active suspension benefits may be significantly reduced.

In this paper, we design a model predictive control (MPC) that provides vehicle drivability while simultaneously improving passenger comfort by reducing chassis motion. Our controller incorporates a reference governor (RG) (Garone et al., 2017) that modifies driver commands when necessary to ensure lateral stability, so that, for instance, the controller prevents the vehicle from losing stability due to driver oversteering. We validate the controller in high-fidelity CarSim simulations, that show (a) reduced chassis motion that improves comfort, (b) improved drivability (responsiveness to the driver commands), and (c) improved vehicle stability on low-friction roads. The simulations also demonstrate the controller robustness to the modeling errors, here caused by the differences between the simple control-oriented model used for prediction and the high-fidelity simulation model.

The paper is organized as follows. Section 2 reviews the control-oriented models, Section 3 proposes a rate-based model predictive control (rate-based MPC) design for tracking the driver commands and reducing the chassis motion. Closed-loop simulation with a CarSim model are reported in Section 4 and conclusions in Section 5.

*Notation:* for a continuous time signal  $x$  sampled with period  $T_s$ ,  $x_t$  denotes the value of the signal at the  $t^{\text{th}}$  step, and  $x_{k|t}$  denotes the value predicted  $k$  steps ahead from  $t$ , i.e.,  $x(t+k)$ .  $\mathbb{R}$ ,  $\mathbb{Z}$  are the set of real and integer number and we use notations such as  $\mathbb{R}_+$ ,  $\mathbb{R}_{0+}$  to denote positive and non-negative numbers. The set operators  $\oplus$ ,  $\ominus$ ,  $\text{co}()$  are the Minkowski sum, Pontryagin difference and convex hull, respectively.  $I_n$  and  $0_n$  are the identity and the zero matrix of dimension  $n$ , respectively, where we drop  $n$  when clear from the context.  $(x, y)$  indicates the stacking of vectors  $x$ ,  $y$ .

## 2. CONTROL ORIENTED VEHICLE DYNAMICS AND SUSPENSION MODEL

The motion model of vehicle and chassis is based on our previous work (Chen et al., 2020), See Fig. 1, 2, where the assumptions are based on normal driving: linear tire forces, small angles, equal left-right front tire steering angles, large longitudinal velocity, and small lift motion. For compactness, we use as sign convention for front/rear wheel base  $b_j$ ,  $j \in \{f, r\}$ ,  $b_f > 0$ ,  $b_r < 0$ , and for left/right track width  $L_{j,i}$ ,  $i \in \{l, r\}$ ,  $L_{j,l} > 0$ ,  $L_{j,r} < 0$ .

### 2.1 Vehicle Dynamics

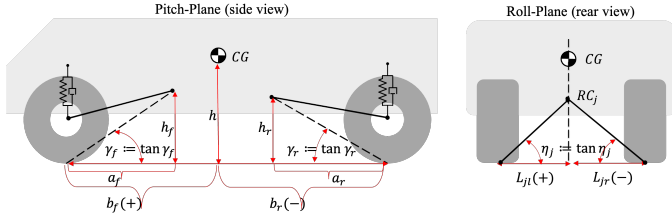


Fig. 1. Trailing arms and parameter definition.

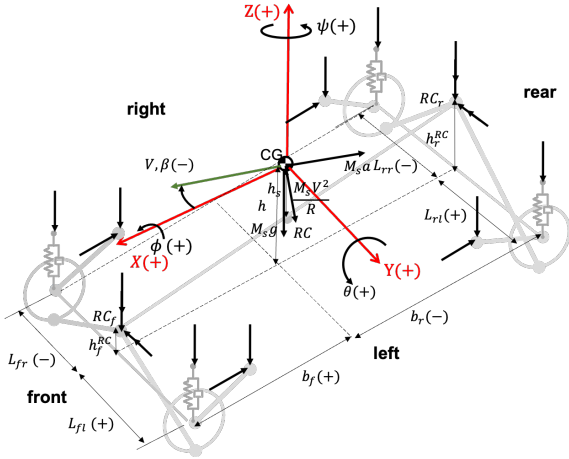


Fig. 2. Free-body diagram of the Sprung-mass and suspension assemblies. Forces' names are omitted for simplicity.

The primary objective is to maintain drivability by tracking the acceleration and steering commands from the driver. The longitudinal acceleration  $a_x$  is modeled by

$$M a_x = \sum_{i=l,r} (u_{fi}\beta + C_f^\alpha \alpha_f) \delta + \sum_{j=f,r} (u_{ji} - C_j^\alpha \alpha_j \beta) \quad (1)$$

where  $j \in \{f, r\}$ ,  $i \in \{l, r\}$ ,  $M$  denotes the sprung mass,  $\beta$  is the body slip angle,  $\alpha_j$  is the tire slip angle, and  $C_j^\alpha$  is the tire cornering stiffness. In (1), the tire traction forces  $u_{ji}$  and the steering angle  $\delta$  are control inputs. The tire slip angles are

$$\alpha_f = \beta + \frac{b_f}{v_x} \dot{\psi} - \delta, \quad \alpha_r = \beta + \frac{b_r}{v_x} \dot{\psi}, \quad (2a)$$

where  $b_j$  is the wheel base,  $v_x$  is the longitudinal velocity, and  $\dot{\psi}$  is the yaw-rate of the sprung mass. The dynamics of the body slip angle  $\beta = \tan^{-1}(v_y/v_x)$  are modeled by

$$v_x \dot{\beta} = -v_x \dot{\psi} - a_x \beta + \frac{1}{M} \sum_{i=l,r} (u_{fi} \delta - \sum_{j=f,r} C_j^\alpha \alpha_j) \quad (3a)$$

and the dynamics of the yaw-rate  $\dot{\psi}$  are modeled by

$$J_Z \ddot{\psi} = \sum_{i=l,r} b_f u_{fi} \delta - \sum_{j=f,r} (b_j C_j^\alpha \alpha_j + L_{ji} u_{ji}), \quad (3b)$$

where the first term is due to steering, the second term is due to the front-rear tire slips difference, and the last term is due to left-right traction forces difference. In what follows, we call  $x_d = [\beta \dot{\psi}]^T$  the *drivability state*.

The secondary objective is to improve passenger comfort in terms of the vehicle chassis motion. The motion of the chassis height  $z$  is modeled by

$$\begin{aligned} M \ddot{z} = & - \sum_{i,j} (K_{ji}(z - b_j \theta) + C_{ji}(\dot{z} - b_j \dot{\theta})) \\ & - \sum_{i,j} (\text{sign}(b_j) \gamma_j u_{ji} + \gamma_f C_f \alpha_f \delta) \\ & - \sum_{i=l,r} \text{sign}(L_{fi}) \eta_j u_{fi} \delta + \sum_{i,j} K_{ji} d_{ji} + C_{ji} \dot{d}_{ji} \end{aligned} \quad (3c)$$

where  $K_{ji}$  ( $K_{ji} = K_j$ ),  $C_{ji}$  ( $C_{ji} = C_j$ ) are the suspension spring stiffness, damping coefficient, respectively,  $d_{ji}$  is the road height at each tire with respect to the nominal and,  $\gamma_j \approx \tan(\gamma_j)$  is the anti-dive/squat angle of the side-view trailing arm,  $\eta_j \approx \tan(\eta_j)$  is the angle between the trailing arm and the ground in the roll plane, see Fig. 1. The first term models the suspension forces, the second term gives the nominal anti-dive and anti-squat forces, the third term models anti-dive and anti-squat forces for non-zero steering angle, and the fourth term gives the road forces.

The motion of the vehicle pitch  $\theta$  is modeled by

$$\begin{aligned} J_Y \ddot{\theta} = & \sum_{i,j} K_{ji} b_j (z - b_j \theta) + C_{ji} b_j (\dot{z} - b_j \dot{\theta}) \\ & + \sum_j (\gamma_j (|b_j| - a_j) - h + h_j) (C_f^\alpha \alpha_f + \sum_i u_{ji}) \\ & + \sum_{i=l,r} b_f \text{sign}(L_{fi}) \eta_f u_{fi} \delta - \sum_{i,j} K_{ji} b_j d_{ji} - C_{ji} b_j \dot{d}_{ji} \end{aligned} \quad (3d)$$

where  $a_j$  is the longitudinal distance between the wheel contact point and the pitch-plane trailing arm mounting point,  $h_j$  is the height of the pitch-plane trailing arm mounting point,  $h$  is the height of CG to the ground when vehicle is stationary, see Fig. 1. The first line models the suspension moments, the second and third lines the anti-dive/squat moments for zero and non-zero steering angles, respectively, and the fourth line the road moments.

The motion of the vehicle roll  $\phi$  is modeled by

$$\begin{aligned} J_X \ddot{\phi} = & - \sum_{i,j} (K_{ji} L_{ji}^2 \phi + C_{ji} L_{ji}^2 \dot{\phi}) \\ & - \sum_i (\text{sign}(b_j) \gamma_j L_{ji} u_{ji} + (h - h_j^{RC}) C_j^\alpha \alpha_j) \\ & + \sum_{i,j} K_{ji} L_{ji} d_{ji} + C_{ji} L_{ji} \dot{d}_{ji} \end{aligned} \quad (3e)$$

where the first line models the suspension moments, the second line the anti-dive/squat moments, and the last line the road torques. The states in (3c), (3d), (3e) are collected into  $x_c = [z \dot{z} \theta \dot{\theta} \phi \dot{\phi}]^T$ , which we call the *comfort state*.

The full state of the model (3) is composed of the drivability state and the comfort state  $x = [x_d^T \ x_c^T]^T = [z \ \dot{z} \ \theta \ \dot{\theta} \ \phi \ \dot{\phi} \ \beta \ \dot{\psi}]^T$ , the control input vector is composed of traction forces and the steering input  $u = [u_{fr} \ u_{fl} \ u_{rr} \ u_{rl} \ \delta]^T$ , and the disturbance vector contains the road heights and their derivatives  $d = [d_{fr} \ d_{fl} \ d_{rr} \ d_{rl} \ \dot{d}_{fr} \ \dot{d}_{fl} \ \dot{d}_{rr} \ \dot{d}_{rl}]^T$ . In (3) the nonlinearities are the bilinear terms between steering angle  $\delta$  and either the body slip angle  $\beta$  or the traction forces  $u_{ji}$ .

The anti-dive/squat suspension geometry determined by  $\gamma_f$ ,  $\gamma_r$ ,  $\eta_f$  can be exploited to use the traction forces  $u_{ji}$

to reduce the motion of chassis height  $z$ , pitch  $\theta$ , and roll  $\phi$  due to the road roughness  $d_{ij}$ ,  $\dot{d}_{ij}$ . While here, we assume a preview for the road roughness, e.g., by cameras and other sensors, a standard e.g., constant, prediction model for  $d$ , can be used when such preview is not available.

## 2.2 Vehicle Constraints

For each tire, the total cannot exceed the friction limit

$$u_{ji}^2 + (C_f^\alpha \alpha_j)^2 \leq (\mu N_{ji})^2, \quad (4)$$

where  $\mu$  is the road-tire friction coefficient,  $N_{ji}$  is the normal force on the tire

$$\begin{aligned} N_{fi} &= \bar{N}_f - K_{fi}(z - b_f\theta + L_{fi}\phi - d_{fi}) \\ &\quad - C_{fi}(\dot{z} - b_f\dot{\theta} + L_{fi}\dot{\phi} - \dot{d}_{fi}) \\ &\quad - \gamma_f(u_{fi} + C_f^\alpha \alpha_f \delta) + \text{sign}(L_{fi})\eta_f(u_{fi}\delta + C_f^\alpha \alpha_f) \end{aligned} \quad (5a)$$

$$\begin{aligned} N_{ri} &= \bar{N}_r - K_{ri}(z + b_r\theta + L_{ri}\phi - d_{ri}) \\ &\quad - C_r(\dot{z} + b_r\dot{\theta} + L_{ri}\dot{\phi} - \dot{d}_{ri}) \\ &\quad + \gamma_r u_{ri} + \text{sign}(L_{ri})\eta_r C_r^\alpha \alpha_r, \end{aligned} \quad (5b)$$

and  $\bar{N}_f$  and  $\bar{N}_r$  are the nominal normal-forces on the tires for a stationary vehicle. Thus, (4) gives state-input constraints that limit the tire forces to a circle of radius  $\mu N_{ji}$ , the ‘‘friction circle’’.

Since we consider normal driving conditions, we make the following assumption that simplifies the control design.

*Assumption 1.* There exist lower bounds  $\underline{N}_{fi} \leq N_{fi}$  and  $\underline{N}_{ri} \leq N_{ri}$  on the normal-forces (5).

Assumption 1 allows to (conservatively) satisfy (4) while ignoring the effects from  $x_c$ . This assumption is implicit when the chassis is not modeled, e.g. (Ren et al., 2016).

In addition to (4) we enforce constraints ensuring the validity model (3) assumptions. Hence, we state and input must be in a region  $\mathbb{T}$  where the tire forces are linear

$$\mathbb{T} = \left\{ \begin{bmatrix} x \\ u \end{bmatrix} : \begin{array}{l} |\beta| \leq \beta^{\max}, |\dot{\psi}| \leq \dot{\psi}^{\max}, |\delta| \leq \delta^{\max} \\ |\alpha_f| \leq \alpha_f^{\max}, |\alpha_r| \leq \alpha_r^{\max} \end{array} \right\}. \quad (6)$$

which involves the drivability state  $x_d$  and the steering input  $\delta$ . For the bound on  $\alpha_f^{\max}$ , ( $\alpha_r^{\max}$  is similarly bounded) we consider two cases depending on the road surface

$$\alpha_f^{\max} = \begin{cases} \alpha^{\text{lin}} & \mu \geq \bar{\mu} \\ \frac{\mu}{C_f^\alpha} \left( \frac{|b_r|}{2\sum_j |b_j|} M_s + M_{fi} \right) g & \mu < \bar{\mu}, \end{cases} \quad (7)$$

where the second term is the static tire vertical force distribution. By (7), for high friction  $\mu \geq \bar{\mu}$ , e.g., dry road, we enforce the tire to operate in the linear region, while for low friction  $\mu \leq \bar{\mu}$ , e.g. ice, the bound is the peak force.

## 3. RATE-BASED MPC FOR DRIVABILITY AND COMFORT

We design a rate-based MPC (Pannocchia, 2015; Huang et al., 2016) achieving both drivability and comfort by precisely tracking the driver commands and reducing chassis motion, respectively. By using a prediction model in velocity form rate-based MPC provides integral action, and hence offset-free tracking of constant references. For handling constraints in presence of disturbances, we exploit concepts from tube MPC (Langson et al., 2004) that uses

a disturbance-free prediction model, applies a feedback correction for disturbance compensation, and tightens the constraints so that the nominal trajectory subject to disturbances and with feedback correction satisfies the actual constraints.

### 3.1 Prediction model

For constructing the prediction model we linearize (3) with parameter vector  $\rho = [v_x \ a_x]^T$  and obtain the linear parameter varying (LPV) system

$$x_{t+1} = A(\rho)x_t + B(\rho)u_t + B_d d_t + w_t \quad (8a)$$

$$y_t = C(\rho)x_t + D(\rho)u_t, \quad (8b)$$

where  $y = [a_x \ \dot{\psi}]^T$ ,  $w_t \in \mathcal{W}$ , which here is a disturbance and ignored in the nominal prediction model, contains the linearization error and possibly the prediction error on the disturbance vector  $d$ , and the polytope  $\mathcal{W}$  is known.

For handling tracking, we formulate (8) in velocity form

$$\begin{aligned} \xi_{t+1} &= \begin{bmatrix} \Delta x_{t+1} \\ e_{t+1} \end{bmatrix} = \begin{bmatrix} A(\rho) & 0 \\ C(\rho) & I \end{bmatrix} \begin{bmatrix} \Delta x_t \\ e_t \end{bmatrix} + \begin{bmatrix} B(\rho) \\ D(\rho) \end{bmatrix} \Delta u_t \\ &\quad + \begin{bmatrix} B_d \\ 0 \end{bmatrix} \Delta d_t + \begin{bmatrix} I \\ 0 \end{bmatrix} \Delta w_t + \begin{bmatrix} 0 \\ I \end{bmatrix} \Delta r_t \end{aligned} \quad (9)$$

where  $e_t = [a_x - a_x^r \ \dot{\psi} - \dot{\psi}^r]^T$  is the tracking error,  $\Delta x_t = x_t - x_{t-1}$ ,  $\Delta u_t = u_t - u_{t-1}$ ,  $\Delta d_t = d_t - d_{t-1}$ ,  $\Delta w_t = w_t - w_{t-1}$ ,  $\Delta r_t = [a_{x,t}^r - a_{x,t-1}^r \ \dot{\psi}_t^r - \dot{\psi}_{t-1}^r]^T$ . In (9), we have approximated the parameter as constant  $\rho_t \approx \rho_{t-1}$ . In what follows, for shortness we write (9) as

$$\xi_{t+1} = \mathcal{A}(\rho)\xi_t + \mathcal{B}(\rho)\Delta u_t + \mathcal{B}_d \Delta d_t + \mathcal{B}_w \Delta w_t + \mathcal{B}_r \Delta r_t \quad (10)$$

*Remark 1.* More refined linearization methods can be applied, such as linearizing about a predicted trajectory. Our design can still be applied but the the description is significantly more convoluted, due to the time varying constraint sets, and hence it is not shown here.

Since (6) only affects the drivability subsystem for robustifying the constraints we extract from (8) the subsystem corresponding to the drivability state  $x^d$ , the steering input  $\delta$ , and the yaw rate  $\dot{\psi}$

$$x_{t+1}^d = A^d(\rho)x_t^d + B^d(\rho)u_t^d + w_t^d \quad (11a)$$

$$y_t^d = C^d(\rho)x_t^d + D^d(\rho)u_t^d, \quad (11b)$$

where  $u_t^d = \delta_t$ ,  $y_t^d = \dot{\psi}_t$ . In velocity form, while assuming  $\Delta r = 0$ ,  $\Delta d = 0$ , (11) gives the subsystem of (9),

$$\xi_{t+1}^d = \mathcal{A}^d(\rho)\xi_t^d + \mathcal{B}^d(\rho)\Delta u_t^d + \mathcal{B}_w^d \Delta w_t^d \quad (12)$$

where  $\xi^d = (\Delta x^d, e^d) = (\Delta x^d, \dot{\psi} - \dot{\psi}^r)$ ,  $\Delta u^d = \Delta \delta$ . To enforce constraints on (11) we extract its states and inputs from those of (12) as shown in (Betti et al., 2013),

$$\begin{bmatrix} x_k^d \\ \delta_{k-1} \end{bmatrix} = C^*(\rho) \begin{bmatrix} \xi_k^d \\ \dot{\psi}^r \end{bmatrix}, \quad (13)$$

$$\begin{aligned} C^*(\rho) &= \begin{bmatrix} A^d(\rho) & B^d(\rho) \\ 0 & 1 \end{bmatrix} \begin{bmatrix} A^d(\rho) - I & B^d(\rho) \\ C^d(\rho)A^d(\rho) & C^d(\rho)B^d(\rho) \end{bmatrix}^{-1} \begin{bmatrix} I & 0 & 0 \\ 0 & 1 & 1 \end{bmatrix} \\ &= \begin{bmatrix} C_\xi^d(\rho) & C_\psi^d(\rho) \end{bmatrix}. \end{aligned}$$

### 3.2 Local Linear Controller

For compensating the effects of the uncertainty in (8) on the constraints, we design a controller that minimizes

the upper bound of the infinite-horizon LQ cost over all realizations of the plant by solving (Kothare et al., 1996)

$$\begin{aligned} \min_{\varsigma, X, Y} \quad & \varsigma \quad (14a) \\ \text{s.t.} \quad & \begin{bmatrix} X & * & * & * \\ \mathcal{A}^d(\rho_i)X + \mathcal{B}^d(\rho_i)Y & X & * & * \\ Q^{d\frac{1}{2}}X & 0 & \varsigma I & * \\ R^{d\frac{1}{2}}Y & 0 & 0 & \varsigma I \end{bmatrix} \geq 0, \quad \forall i \in \{1, \dots, \ell\} \end{aligned}$$

where  $*$  are the terms completing a symmetric matrix,  $\varsigma \geq 0$ , and  $\rho_i$ ,  $i \in \{1, \dots, \ell\}$  are the parameter values determining vertex matrices  $(\mathcal{A}^d(\rho_i), \mathcal{B}^d(\rho_i))$  such that  $(\mathcal{A}^d(\rho), \mathcal{B}^d(\rho)) \in \text{co}(\{(\mathcal{A}^d(\rho_i), \mathcal{B}^d(\rho_i))\}_{i=1}^{\ell})$  for all admissible value of  $\rho$ .

The solution of (14) produces a state-feedback controller

$$\Delta u_t^d = F_x^d \Delta x_t^d + F_e^d e_t^d \quad (15)$$

for (9) where  $\mathcal{F}^d = [F_x^d \ F_e^d] = YX^{-1}$  is the controller gain and  $P^d = X^{-1}$  defines the Lyapunov function  $\xi_d^T P^d \xi_d$  for the closed-loop system. When applied to (8), (15) results in the proportional-integral controller

$$u_t^d = F_x^d x_t^d + F_e^d \sum_{k=0}^t e_k^d \quad (16)$$

that provides offset-free steady-state tracking of constant references and rejection of constant disturbances. Controller (16) only actuates steering, since this has larger authority on the lateral dynamics, where the uncertainty affects the constraints, and we use the traction forces primarily for longitudinal dynamics and comfort.

### 3.3 Robust constraints

As suggested in (Betti et al., 2013), a less conservative approach for tightening the constraints based on (12) is to include the auxiliary dynamics  $\vartheta_{t+1}^d = \vartheta_t^d$ , where  $\vartheta_t^d = w_{t-1}^d$  so that,  $\Delta w_t^d = w_t^d - \vartheta_t^d$ . Such procedure results in the robust positive invariant (RPI) set  $\mathcal{Z}$  for the augmented system such that

$$\begin{aligned} (\xi^d, \vartheta^d) \in \mathcal{Z} \implies \\ (\mathcal{A}^d(\rho) + \mathcal{B}^d(\rho)\mathcal{F}^d)\xi^d + \mathcal{B}_w^d(w^d - \vartheta^d), w^d \in \mathcal{Z} \\ \forall w^d \in \mathcal{W}^d, \forall \rho \in \text{co}(\{\rho_i\}_{i=1}^{\ell}). \end{aligned} \quad (17)$$

Given a predicted state  $\xi_{k|t}^d$ , computed without disturbances,  $w_{k|t}^d = 0$ , and the corresponding actual state  $\xi_{t+k}^d$ , we have  $(\xi_{t+k}^d, \vartheta_{t+k}^d) \in (\xi_{k|t}^d, 0) \oplus \mathcal{Z}$  for all  $k \in \mathbb{Z}_+$ , whenever  $(\xi_t^d - \xi_{0|t}^d, w_{t-1}^d) \in \mathcal{Z}$  and  $w_{t+k}^d \in \mathcal{W}^d$  for all  $k \in \mathbb{Z}_+$ . Thus, since the constraints (6) only involve elements of (11), we ensure the satisfaction of (6) despite  $w^d \in \mathcal{W}^d$  by enforcing

$$\begin{aligned} C^*(\rho) \begin{bmatrix} \xi_k^d \\ \psi^r \end{bmatrix} \in \mathbb{T} \ominus [C_{\xi}^d(\rho) \ C_w^d(\rho)] \mathcal{Z}, \quad (18) \\ C_w^d(\rho) = \begin{bmatrix} I \\ 0 \end{bmatrix} \\ - \begin{bmatrix} A^d(\rho) & B^d(\rho) \\ 0 & 1 \end{bmatrix} \begin{bmatrix} A^d(\rho) - I & B^d(\rho) \\ C^d(\rho)A^d(\rho) & C^d(\rho)B^d(\rho) \end{bmatrix}^{-1} \begin{bmatrix} I \\ C^d(\rho) \end{bmatrix}. \end{aligned}$$

### 3.4 Yaw rate reference manipulation

In order to increase vehicle stability we provide the rate-based MPC with the capability of manipulating the reference similar to a RG, see, e.g., (Limón et al., 2008).

Since for normal driving conditions loss of stability is primarily caused by the lateral dynamics we consider again the subsystem (11) in velocity form (12). We construct the maximal output admissible set (MOAS) (Garone et al., 2017) for constant reference  $\dot{\phi}^r$ , using the approach in (Betti et al., 2013),

$$\begin{aligned} \mathbb{O} = \left\{ (\xi^d, \dot{\psi}^r) : C_{\psi} \dot{\psi}^r \in \mathbb{T} \ominus \left( [C_{\xi}^d \ C_w^d] \mathcal{Z} \right) \right. \\ \left. C_{\xi}^d (\mathcal{A}^d + \mathcal{B}_u^d \mathcal{F}^d)^k \xi^d + C_{\psi} \dot{\psi}^r \in \mathbb{T} \ominus \left( [C_{\xi}^d \ C_w^d] \mathcal{Z} \right), \forall k \right\}, \quad (19) \end{aligned}$$

for a fixed value of  $\rho = r_0$ , since this will be used for manipulating the reference and such approximation has limited impact, yet allows for much simpler design procedure than a varying  $\rho$ .

*Remark 2.* Due to (7),  $\mathbb{T}$  in (18) and (19) changes. However, the conditions in (7) are kept constant during the prediction horizon. Thus, the sets for the two conditions can be easily precomputed.

### 3.5 Desired Steady-State

Due to having five control inputs and only two references, the yaw rate and the acceleration, the vehicle is over-actuated. To obtain uniqueness of the closed-loop equilibrium, we define additional references for the inputs, namely, that the steady state left-right traction forces are balanced, and the front-rear forces are distributed as the nominal tire normal forces,

$$u_{fi,\infty} = \frac{|b_r|}{2\sum_j |b_j|} M a_x^r, \quad u_{ri,\infty} = \frac{|b_f|}{2\sum_j |b_j|} M a_x^r. \quad (20a)$$

The steady state steering angle is obtained from the (3a), (3b), (2) for a steady state with  $\dot{\psi} = \dot{\psi}^r$ ,

$$\delta_{\infty} = K_{\delta\dot{\psi}}^{-1} \dot{\psi}^r \quad (20b)$$

where  $K_{\delta\dot{\psi}}$  is the steady-state gain of (3a), (3b). The additional references avoid that the closed-loop converges to an undesirable equilibrium, such as one where opposing traction forces or steering angles will be used, which would increase tire wear and consumption.

### 3.6 Robust Rate-based MPC

At each time  $t$  the rate-based MPC solves the constrained finite-time optimal control problem

$$\begin{aligned} \min_{\Delta U_t, \xi_{0|t}^d, \dot{\phi}_t^r} \quad & \|\dot{\phi}_t^r - \dot{\psi}_t^r\|_T^2 + \|\xi_{N|t}\|_P^2 + \sum_{k=0}^{N-1} (\|\xi_{k|t}\|_Q^2 \\ & + \|\Delta u_{k|t}\|_R^2 + \|u_{t-1} + \Delta u_{k|t} - u_{\infty}\|_{R_u}^2) \end{aligned} \quad (21a)$$

$$\text{s.t.} \quad (\xi_{0|t}^d - \xi_t^d, w_{t-1}^d) \in \mathcal{Z}, x_{0|t}^c = x_t^c \quad (21b)$$

$$\hat{e}_{0|t} = e_t + (\dot{\phi}_t^r - \dot{\psi}_t^r) \quad (21c)$$

$$\xi_{k+1|t} = \mathcal{A}(\rho)\xi_{k|t} + \mathcal{B}(\rho)\Delta u_{k|t} + \mathcal{B}_d\Delta d_{k|t} \quad (21d)$$

$$(x_{k|t}^d, \delta_{k-1|t}) \in \mathbb{T} \ominus \left( [C_{\xi}^d(\rho) \ C_w^d(\rho)] \mathcal{Z} \right) \quad (21e)$$

$$u_{t-1} + \sum_{k=0}^{N-1} \Delta u_{k|t} \in \mathbb{U}_t \quad (21f)$$

$$(\xi_{N|t}^d, \dot{\phi}_t^r) \in \mathbb{O} \quad (21g)$$

where  $\Delta U_t = (\Delta u_{0|t}, \dots, \Delta u_{N-1|t})$ ,  $N$  is the prediction horizon,  $P$ ,  $Q$ ,  $R$ ,  $R_u$  are positive definite matrix weights,

$\xi_{k|t}^d$  is the subvector of  $\xi_{k|t}$  for subsystem (12), and  $w_t^d$  is the estimate of the disturbance at time  $t$  which is computed from the current state and its previous prediction,  $w_{t-1}^d = x_t^d - x_{1|t-1}^d$ . In (21) the time varying input constraint set is

$$\mathcal{U}_t = \{u \in \mathbb{R}^5 : |u_{f(r)i}| \leq \min \{u_{f(r)}^{\max}, u_{f(r),k|t}^{\max}\}\} \quad (22)$$

where  $u_{j,k|t}^{\max} = \sqrt{(\mu N_{ji,t})^2 - (C_j^\alpha \alpha_{j,t})^2}$ ,  $j \in \{f, r\}$  reduces the forces bound when necessary due to the friction limit.

Cost (21a) penalizes the tracking error, chassis motion, input deviation from the steady-state computed from (20),  $u_\infty = [u_{fr,\infty} \ u_{fl,\infty} \ u_{rr,\infty} \ u_{rl,\infty} \ \delta_\infty]^T$ , and changes to traction forces and steering angle. The references are assumed constant in prediction so that in (21d),  $\Delta r_{k|t} = 0$ .

The tightened constraints (21e) aim at robust constraint satisfaction. In the terminal constraint (21g) the reference  $\psi^r$  can be modified by  $\varphi_t^r$ , which affects the tracking error via (21c), to increase feasibility for a cost penalty, where  $T$  is an appropriate weight (Limón et al., 2008).

Let the predicted optimal state and input trajectories solving (21) be  $\xi_t^* = (\xi_{0|t}^*, \dots, \xi_{N|t}^*)$ ,  $\Delta U_t^* = (\Delta u_{0|t}^*, \dots, \Delta u_{N-1|t}^*)^*$ , respectively. The rate-based MPC control law is

$$u_t = u_{t-1} + \Delta u_{0|t}^* + \Phi \mathcal{F}^d (\xi_t^d - \xi_{0|t}^{d*}). \quad (23)$$

where  $\Phi$  is a matrix that applies the feedback command to the proper component of the input vector, i.e.,  $\delta$ .

*Remark 3.* Due to the approximations and assumptions made, (21e), (21g) cannot always provide guarantee of constraint satisfaction and recursive feasibility. However, in extensive simulations the approximations appeared to be sufficiently precise, with only rare and minimal constraint violations that are only seen in case of an extremely aggressive tuning, and that are handled in practice by implementing (21e), (21g) as soft constraints.

*Remark 4.* In (23) the feedback term designed in Sec. 3.2 only actuates the steering, since (6) affects only (11) and in (13) the reference and input vectors must have the same size. We can also use a full feedback gain, i.e.,  $\mathcal{F}(\xi_t - \xi_{0|t}^*)$  designed by (14) for (9), as long as  $\mathcal{Z}$  remains a subset of an RPI for the modified closed-loop system, and the steering actuation is not larger than that of  $\mathcal{F}^d$ . These conditions usually hold, since  $\mathcal{F}$  has larger authority than  $\mathcal{F}^d$ , and hence provides better disturbance rejection (smaller RPI) and less steering actuation (due to more available inputs).

#### 4. CLOSED-LOOP SIMULATIONS IN CARSIM

In this section we validate our rate-based MPC (23) through simulations. The closed-loop simulations are executed in Simulink/Matlab using a high precision EV model developed in CarSim, where the suspension geometry of the default CarSim model has been modified to more closely representing today's anti-dive/squat suspension, according to the models in Section 2, which are closer to real suspensions. We consider different simulation scenarios, with lane change and acceleration/deceleration maneuvers under high and low friction-coefficient, and smooth and rough road surfaces. We compare the closed-loop behavior obtained with the rate-based MPC designed

in Section 3, with the CarSim default speed and steering controller with preview as baseline, which we consider representative of conventional controllers for EV.

The controller sampling period is  $T_s = 0.01$  s, while the closed-loop CarSim simulation has an update frequency at least 20 times higher. The prediction horizon is  $N = 5$  steps, which provides a reasonable balance between performance and computational burden, and the parameter vector value for terminal set design is  $\rho_0 = (15\text{m/s}, 0)$ .

##### 4.1 Rough road disturbance rejection

To evaluate the controller's performance in passenger comfort improvement, we consider a straight line, constant speed driving on a rough road. The road roughness profile is shown in Fig. 3, the road friction coefficient is  $\mu = 0.9$  and the initial vehicle velocity is  $v_x(0) = 15$  m/s.

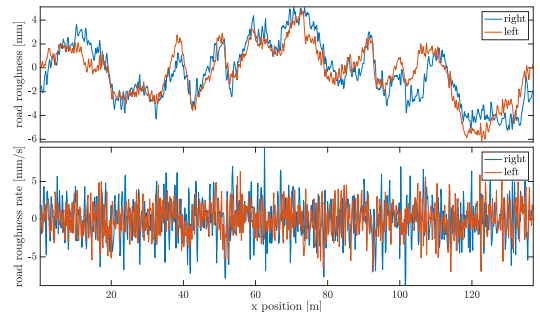
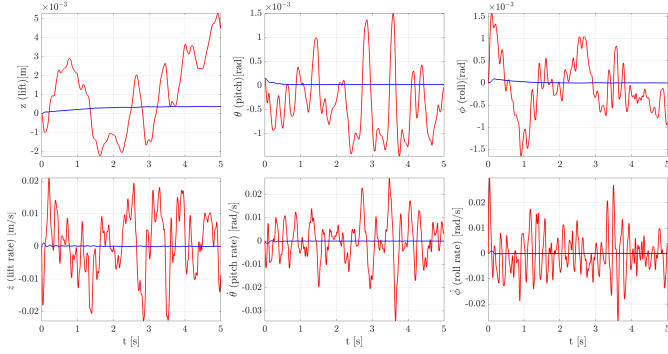


Fig. 3. Road roughness profile for disturbance rejection test. Road height and height rate at right (blue) and left (left) wheels.

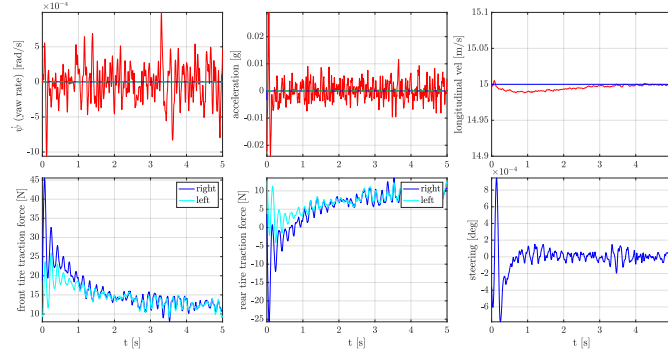
The results for this simulation scenario are shown in Fig. 4. Figure 4a shows the time domain response of the chassis lift  $z$ , pitch  $\theta$ , and roll  $\phi$  motions characterizing the passenger comfort. Figure 4b shows the tracking performance for both yaw rate  $\dot{\psi}$  and longitudinal acceleration  $a_x$ , the longitudinal velocity  $v_x$  and the longitudinal force of each tire  $u_{ji}$ ,  $j \in \{f, r\}$ ,  $i \in \{l, r\}$ , the front steering angle  $\delta_f$ <sup>1</sup>.

As it can be observed in Fig. 4a, the chassis motion is significantly reduced with the rate-based MPC controller compared to that with the default CarSim controller, demonstrating the capability of the rate-based MPC in improving passenger comfort in the presence of the rough road. Fig. 4b shows that the rate-based MPC controller uses the anti-lift/squat suspension to create forces to counteract the road forces, as originally suggested in (Chen et al., 2020), that results in reduced chassis motion. Fig. 4b shows that the rate-based MPC controller improves the tracking performance of yaw rate and longitudinal acceleration with respect to the CarSim baseline controller, since the latter is more affected by the rough road disturbances. Although preview on road roughness, which was shown to be achievable to high accuracy, see, e.g., (Tudón-Martínez et al., 2015), improves performance, in our tests the controller worked well even when such preview was not used.

<sup>1</sup> For the CarSim baseline controller the single tire forces and front tire steering angle are not shown because the CarSim controller commands the total torque and the steering wheel angle.



(a) Chassis motion: lift, pitch, roll (and derivatives).



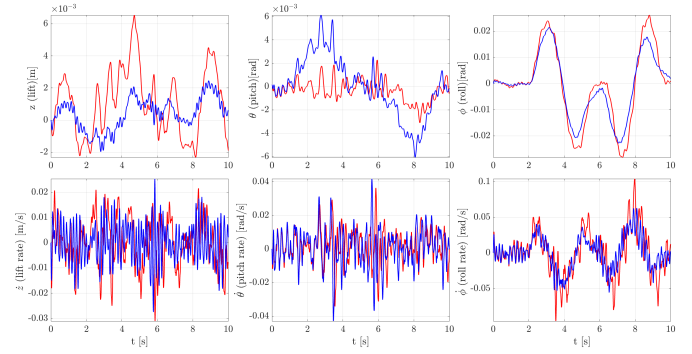
(b) Vehicle yaw rate, acceleration, longitudinal velocity, tire forces, front tire steering angle.

Fig. 4. Simulation results for rough road disturbance rejection: CarSim baseline controller (red), rate-based MPC controller (blue), reference trajectories (dash-green). For the scenario of straight driving at constant speed,  $a_x^r = 0$  and  $\psi^r = 0$ .

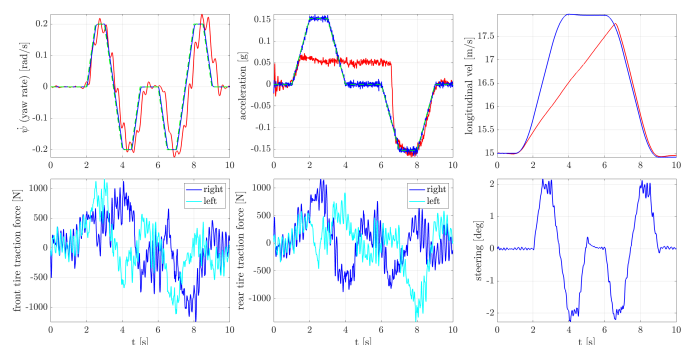
#### 4.2 Double lane change on a high friction rough road

Next, we consider a fast double lane change maneuver on a rough road to evaluate the controller performance in reference tracking and passenger comfort improvement in a challenging condition. The road roughness profile is the same as shown in Fig. 3. The road friction coefficient is  $\mu = 0.9$ . The initial condition of the scenario is straight driving at 15 m/s (54 km/h). After 2 s, the desired yaw rate ramps up to 0.2 rad/s (left turn), and the desired acceleration ramps up to 1.5 m/s<sup>2</sup>. After 3 s, the desired yaw rate ramps down to -0.2 rad/s (from left turn to right turn), and the desired longitudinal acceleration ramps down to zero. From 4 to 6 s, the desired vehicle speed is constant, and the desired yaw rate is first kept to be -0.2 rad/s for 0.5 s, and then ramps up back to zero at 5s and is kept zero until 6 s. After 6 s, the desired yaw rate ramps down again to -0.2 rad/s (right turn) and held constant for 0.5 s. The desired acceleration ramps down to -1.5 m/s<sup>2</sup> and is held constant for 0.5 s until 8 s. After 7 s, the desired yaw rate ramps up to 0.2 rad/s (from right to left turn), held constant for 0.5 s and then ramps up to 0.2 rad/s. After 8 s, the desired longitudinal acceleration ramps up to zeros and is held constant after that. The desired yaw rate is held to 0.2 rad/s for 0.2 s and then ramps down to 0 at 9 s and remain that afterwards.

The results for this simulation scenario are shown in Fig. 5, which has the same structure and notation as Fig. 4. As shown in Fig. 5b, the rate-based MPC achieves precise tracking of longitudinal acceleration and yaw rate



(a) Chassis motion: lift, pitch, roll (and derivatives).



(b) Vehicle yaw rate, acceleration, longitudinal velocity, tire forces, front tire steering angle.

Fig. 5. Simulation results for double lane change on a rough road with high friction: CarSim baseline controller (red), rate-based MPC controller (blue), reference trajectories (dash-green).

as opposed to the CarSim baseline controller which has a significantly lower performance, due to the challenging scenario. As for driver comfort, Fig.5a shows that the rate-based MPC reduces both the chassis lift and roll motions a when compared to the CarSim baseline controller, but the pitch angle increases with the rate-based MPC. This is due to the suspension geometry that makes lift and pitch reduction conflicting goals when the vehicle accelerates/decelerates. Since the CarSim controller achieves a worse tracking of the acceleration signal, reducing the acceleration from the reference, also reduces the pitch. Instead in order to achieve better yaw rate and acceleration tracking while reducing roll and lift, the rate-based MPC sacrifices a little the pitch performance, since improving all objectives is impossible.

#### 4.3 Double lane change, on a low friction smooth road

Finally, we consider a double lane change maneuver on a smooth road with a low friction coefficient,  $\mu = 0.3$ , in order to evaluate the controller's performance in maintaining handling stability in a challenging condition. The desired longitudinal acceleration during the test is  $a_x^r = 0$ , i.e., constant speed. The initial condition is straight driving at 15 m/s (54 km/h). After 2 s, the desired yaw rate ramps up to reach 0.3 rad/s (left turn) at 3 s and is held constant for 2 s. After 5 s, the desired yaw rate ramps down to zero and keeps constant for 2 s. After 6 s, the desired yaw rate ramps down to -0.3 rad/s and keeps constant for 2 s. After 11 s, the desired yaw rate ramps up to zero and then remains that afterwards.

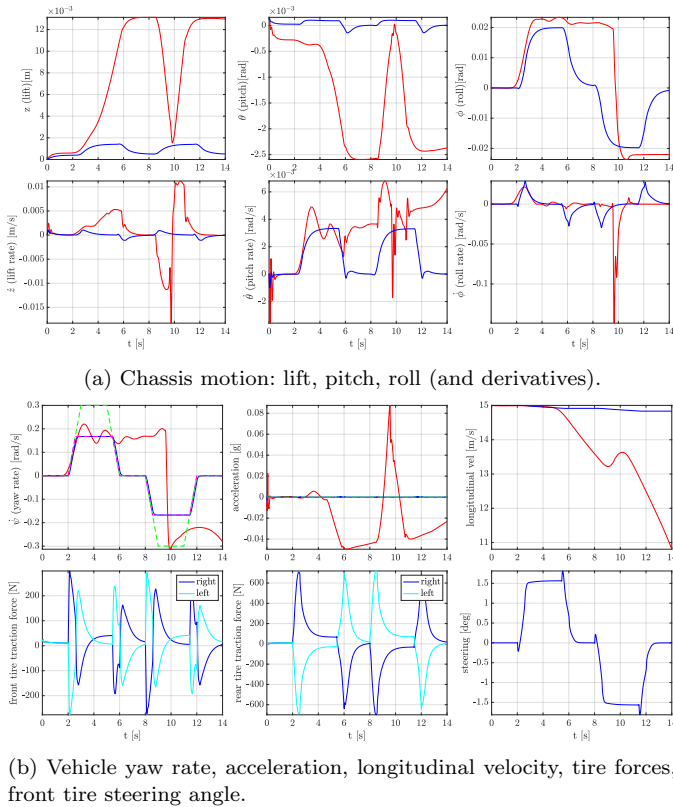


Fig. 6. Simulation results for double lane change on a smooth road with low friction: CarSim baseline controller (red), rate-based MPC controller (blue), reference trajectories (dash-green), references modified within the rate-based MPC (dash-magenta), based on MOAS.

Figure 6a shows the results on this maneuver for the rate-based MPC and the default CarSim controller, with the same structure and notation as Fig. 4. Fig.6b shows that since the yaw rate reference is too high for the low friction of the road, when the default CarSim controller is used, the vehicle starts to lose stability after 10 s. On the other hand, when the rate-based MPC controller is used, the yaw rate reference is adequately reduced by (21g) based on the achievable set-point. As a result, the rate-based MPC can maintain handling stability.

## 5. CONCLUSIONS

This paper presents the design of a rate-based MPC for controlling EVs with independent wheel motors aimed at simultaneously achieving drivability, i.e., responsive longitudinal acceleration and yaw rate tracking, and passenger comfort, i.e., reduced chassis relative motion. We have evaluated the rate-based MPC controller in closed-loop simulations with a high fidelity CarSim model in different maneuvers and road conditions. The results showed improvements with respect to a baseline CarSim controller, representative of conventional controllers in EV, in terms of reference tracking, passenger comfort improvement, and lateral stability.

## REFERENCES

Betti, G., Farina, M., and Scattolini, R. (2013). A robust MPC algorithm for offset-free tracking of constant ref-

erence signals. *IEEE Trans. Automatic Control*, 58(9), 2394–2400.

Chen, D., Danielson, C., and Iezawa, M. (2020). Improving passenger comfort by exploiting hub motors in electric vehicles: Suspension modeling. In *Dynamic Systems and Control Conference*.

Garone, E., Di Cairano, S., and Kolmanovsky, I. (2017). Reference and command governors for systems with constraints: A survey on theory and applications. *Automatica*, 75, 306–328.

Huang, M., Zaseck, K., Butts, K., and Kolmanovsky, I. (2016). Rate-based model predictive controller for diesel engine air path: Design and experimental evaluation. *IEEE Trans. Control Systems Tech.*, 24(6), 1922–1935.

Kothare, M.V., Balakrishnan, V., and Morari, M. (1996). Robust constrained model predictive control using linear matrix inequalities. *Automatica*, 32(10), 1361–1379.

Langson, W., Chrysochoos, I., Raković, S., and Mayne, D.Q. (2004). Robust model predictive control using tubes. *Automatica*, 40(1), 125–133.

Limón, D., Alvarado, I., Alamo, T., and Camacho, E.F. (2008). MPC for tracking piecewise constant references for constrained linear systems. *Automatica*, 44(9), 2382–2387.

Nahidi, A., Kasaiezadeh, A., Khosravani, S., Khajepour, A., Chen, S.K., and Litkouhi, B. (2017). Modular integrated longitudinal and lateral vehicle stability control for electric vehicles. *Mechatronics*, 44, 60–70.

Ochi, N., Fujimoto, H., and Hori, Y. (2013). Proposal of roll angle control method using positive and negative anti-dive force for electric vehicle with four in-wheel motors. In *IEEE Int. Conf. Mechatronics*, 816–821.

Pannocchia, G. (2015). Offset-free tracking MPC: A tutorial review and comparison of different formulations. In *2015 European Control Conf.*

Ren, B., Chen, H., Zhao, H., and Yuan, L. (2016). MPC-based yaw stability control in in-wheel-motored ev via active front steering and motor torque distribution. *Mechatronics*, 38, 103–114.

Tudón-Martínez, J.C., Fergani, S., Sename, O., Martínez, J.J., Morales-Menendez, R., and Dugard, L. (2015). Adaptive road profile estimation in semiactive car suspensions. *IEEE Trans. Control Systems Technology*, 23(6), 2293–2305.

Wang, R., Zhang, H., Wang, J., Yan, F., and Chen, N. (2015). Robust lateral motion control of four-wheel independently actuated electric vehicles with tire force saturation consideration. *Jour. of the Franklin Institute*, 352(2), 645–668.

Zhang, H. and Wang, J. (2015). Vehicle lateral dynamics control through AFS/DYC and robust gain-scheduling approach. *IEEE Trans. Vehicular Tech.*, 65(1), 489–494.

Zhao, H., Chen, W., Zhao, J., Zhang, Y., and Chen, H. (2019). Modular integrated longitudinal, lateral, and vertical vehicle stability control for distributed electric vehicles. *IEEE Trans. Vehicular Tech.*, 68(2), 1327–1338.